Linear high-resolution schemes for hyperbolic conservation laws: TVB numerical evidence [1]

C. Bona [a,2], C. Bona-Casas [a,3], J. Terradas [b,4]

[a]*Departament de Física. Universitat de les Illes Balears.*
Institute for Applied Computation with Community Code (IAC^3)

[b]*Centre for Plasma Astrophysics, Katholieke Universiteit Leuven, Celestijnenlaan*
200B, B-3001 Leuven, Belgium

Abstract

The Osher-Chakrabarthy family of linear flux-modification schemes is considered. Improved lower bounds on the compression factors are provided, which suggest the viability of using the unlimited version. The LLF flux formula is combined with these schemes in order to obtain efficient finite-difference algorithms. The resulting schemes are applied to a battery of numerical tests, going from advection and Burgers equations to Euler and MHD equations, including the double Mach reflection and the Orszag-Tang 2D vortex problem. Total-variation-bounded behavior is evident in all cases, even with time-independent upper bounds. The proposed schemes, however, do not deal properly with compound shocks, arising from non-convex fluxes, as shown by Buckley-Leverett test simulations.

Key words: Hyperbolic conservation laws, Numerical methods
PACS: 47.11Df, 47.11Bc

1 Introduction

The study of hyperbolic conservation laws, as described by

$$\partial_t u + \partial_x f(u) = 0 \ , \tag{1}$$

is a classical topic in Computational Fluid Dynamics (CFD). We have noted here by u a generic array of dynamical fields, and we will assume strong hyperbolicity, so that the characteristic matrix

$$A(u) = \partial f / \partial u \tag{2}$$

has real eigenvalues and a full set of eigenvectors.

As it is well known, the system (1) admits weak solutions, so that the components of u may show piecewise-smooth profiles. Standard finite-difference schemes, like the Lax-Wendroff [1] or MacCormack [2] ones, produce spurious overshots and oscillations at non-smooth points which can mask the physical solutions, even leading to code crashing. These deviations do not diminish with resolution, in analogy with the Gibbs phenomenon found in the Fourier series development of discontinuous functions.

This difficulty was overcome in the pioneering work of Godunov [3]. On a uniform computational grid $x_j = j\triangle x$, equation (1) can be approximated by the semi-discrete equation

$$\partial_t u_j = -\frac{1}{\Delta x} \left(h_{j+1/2} - h_{j-1/2} \right) \ , \tag{3}$$

where the interface flux $h_{j+1/2}$ is computed by an upwind-biased formula from the neighbor grid nodes. In the scalar case, one can define the total variation of a discrete function as

$$TV(u) = \sum_j | u_j - u_{j-1} | \ . \tag{4}$$

In the case of systems, the total variation is defined as the sum of the total variation of the components. Godunov scheme is total-variation-diminishing (TVD), meaning that $TV(u)$ does not increase during numerical evolution. It is obvious that TVD schemes can not develop spurious oscillations: monotonic initial data preserve their monotonicity during time evolution. Moreover, the TVD property can be seen as a strong form of stability: any blow-up of the numerical solution is excluded, as far as it would increase the total variation.

Godunov scheme is the prototype of the so-called upwind-biased schemes, which require either the exact or some approximate form of spectral decomposition of the characteristic matrix (2). This makes them both computationally expensive and difficult to extend to the multidimensional case. A much simpler alternative is provided by the local Lax-Friedrichs (LLF) scheme (Rusanov scheme [4])

$$h_{j+1/2} = \frac{1}{2} \left[f_{j+1} + f_j - \lambda_{j+1/2} \left(u_{j+1} - u_j \right) \right] , \tag{5}$$

where λ is the spectral radius of the characteristic matrix and we have taken

$$\lambda_{j+1/2} = max(\lambda_j, \lambda_{j+1}) . \tag{6}$$

The LLF scheme is the prototype of the so-called centered schemes, which deserve a revived interest nowadays in view of multidimensional applications. It clear from (3, 5) that the LLF scheme, like the Godunov one, is only first-order accurate in space. Second-order accuracy can be obtained following the Harten modified-flux approach [5], which was soon extended to very-high accuracy (up to 15th order) by Osher and Chakrabarthy [6]. The basic idea is to replace the lower order TVD flux $h_{j+1/2}$ by a modified flux $f_{j+1/2}$, obtained by some interpolation procedure involving a higher number of nodes.

All these high-resolution schemes require some form of flux-correction limiters in order to ensure the TVD property. As a consequence, accuracy is reduced to (at most) first order at non-sonic critical points, where the limiters come into play. In order to circumvent this problem, one can relax the TVD condition, demanding instead that the total variation is bounded, that is

$$TV(u) \leq B , \tag{7}$$

where the upper bound B is independent of the resolution, but could depend on the elapsed time. Even if we are ready to relax the stronger TVD requirement, keeping the bound (7) is important from the theoretical point of view. One major advantage of total-variation-bounded (TVB) schemes is that there is a convergent (in L_{loc}^1) subsequence as $\Delta x \to 0$ to a weak solution of (1). If an additional entropy condition is satisfied, then the proposed scheme is convergent (see for instance Ref. [7]).

An interesting example of such TVB schemes was given by Shu [8], by softening the flux limiters proposed in Ref. [6]. Although the TVB property is proven for the schemes presented in [8], based on a linear flux-modification procedure, a rigorous proof is still unavailable for more complex cases. An important example is provided by the essentially-non-oscillatory (ENO) methods [9] [10],

where the TVD property is relaxed in a different way. Numerical evidence shows that ENO schemes, as well as their weighted-ENO variants [11]-[13], deserve their name: the TVB property is satisfied in practice, even with time-independent bounds. An implementation of these high-resolution methods for the LLF Flux is given in Refs. [14] [15].

In this paper we consider (the unlimited version of) the 'β-family' of Osher-Chakrabarthy linear flux-modification algorithms in the semidiscrete framework. The choices of the β parameter are optimized for their use with the unlimited version, by refining the bounds given in the original paper [6]. As a lower order TVD flux, we will use the standard LLF one (5). The resulting high-resolution schemes can then be recast into a compact finite-difference formula. This greatly increases computational efficiency, specially with a view to three-dimensional applications. We perform a battery of standard tests in one space dimension, covering advection, Burgers and Euler equations, in order to show that the TVB property is fulfilled in practice for the selected values of the β parameter. We are not able, however, of getting the right result for compound shocks, arising from non-convex fluxes; this is illustrated by the Buckley-Leverett test simulations. We also consider some multidimensional tests cases with the Euler and magneto-hydrodynamics (MHD) equations, including the double Mach reflection and the Orszag-Tang 2D vortex problem. Total-variation-bounded behavior is evident in all the proposed cases, even with time-independent upper bounds.

2 The Osher-Chakravarthy β-schemes

Following Ref. [6], let us consider the centered $2m - 1$ order schemes:

$$\partial_t u_j = -C^{2m} f_j + (-1)^{m-1} \beta (\Delta x)^{2m-2} D_+^m D_-^{m-1} (df_{j-1/2}^+ - df_{j-1/2}^-) , \qquad (8)$$

where C^{2m} is the central $2m$th-order-accurate difference operator with a stencil of $2m + 1$ grid points, and we have used the standard notation $D_\pm$ for the elementary difference operators. The flux differences $df^\pm$ are defined as follows:

$$df_{j+1/2}^+ = f_{j+1} - h_{j+1/2} \qquad df_{j+1/2}^- = h_{j+1/2} - f_j , \qquad (9)$$

where $h_{j+1/2}$ is any (lowest-order) TVD flux. The β parameter in the dissipative term in (8) is assumed to be positive: a necessary condition for stability.

The algorithms (8) can be put into an explicit flux-conservative form by replacing the lowest order flux $h_{j+1/2}$ in (3) by [6] [8]

$$f_{j+1/2} = h_{j+1/2} + \sum_{k=-m+1}^{m-1} \left(c_k^m \, df_{j+k+1/2}^- + d_k^m \, df_{j+k+1/2}^+ \right) , \tag{10}$$

where

$$d_k^m = \nu_k^m - (-1)^k \beta \begin{pmatrix} 2m-2 \\ k+m-1 \end{pmatrix} , \qquad c_k^m = -d_{-k}^m \tag{11}$$

(we use here a compact notation), and

$$\nu_0^m = 1/2 , \qquad \nu_k^m = -\nu_{-k}^m \qquad (k \neq 0) \tag{12}$$

$$\nu_{m-1}^m = (-1)^{m-1} \left[m \begin{pmatrix} 2m \\ m \end{pmatrix} \right]^{-1} \qquad (m > 1) \tag{13}$$

$$\nu_k^{m+1} = \nu_k^m + (-1)^k \frac{k}{m} \begin{pmatrix} 2m \\ m-k \end{pmatrix} \left[(m+1) \begin{pmatrix} 2m+2 \\ m+1 \end{pmatrix} \right]^{-1} . \tag{14}$$

The TVD property is enforced by limiting the flux differences $df^\pm$ (see [6], [8] for the details). As a generic example, $df_{j+k+1/2}^+$ in (10) is replaced by

$$minmod(\, df_{j+k+1/2}^+, bdf_{j+1/2}^+, bdf_{j-1/2}^+ \,), \tag{15}$$

where b is a compression factor. This replacement introduces a non-linear component in the linear flux-correction formula (10). The resulting scheme will be TVD if and only if:

$$C_{j+1/2} \equiv 1 + \sum_{k=-m+1}^{m-1} c_k^m \, \frac{df_{j+k+1/2}^- - df_{j+k-1/2}^-}{df_{j+1/2}^-} \geq 0 \tag{16}$$

$$D_{j-1/2} \equiv 1 + \sum_{k=-m+1}^{m-1} d_k^m \, \frac{df_{j+k+1/2}^+ - df_{j+k-1/2}^+}{df_{j-1/2}^+} \geq 0 . \tag{17}$$

$$\lambda_j \frac{\Delta t}{\Delta x} (C_{j+1/2} + D_{j+1/2}) \leq 1 , \tag{18}$$

where we have assumed a time discretization based on the forward Euler step, so that the last condition provides an upper bound on the time step Δt.

5

3 Compression factor optimization

In the original paper [6], the ansatz

$$\beta \leq [\, m \begin{pmatrix} 2m \\ m \end{pmatrix} \,]^{-1} \tag{19}$$

was used for getting a sufficient condition from (16, 17), amounting to a simple constraint on the range of the compression parameter b

$$0 \; < \; b \; \leq \; [\, 1 + 2\beta \begin{pmatrix} 2m - 2 \\ m - 1 \end{pmatrix} \,]\, [\, \sum_{j=2}^{m} \frac{1}{2j - 1} \,]^{-1} \; . \tag{20}$$

Allowing for (20), the upper bound b_{max} increases with β, which is in turn bounded by (19). For the third-order scheme ($m = 2$), the optimal choice would then be $\beta = 1/12$, so that the compression parameter may reach $b_{max} = 4$, still preserving the TVD property. This means that, for monotonic profiles, the flux-correction limiters would act only where the higher order corrections in neighboring computational cells differ at least by a factor of four. This is not to be expected in practical, good resolution, simulations of smooth profiles, even when large gradients appear. This high-compression-factor property can be at the origin of the robust behavior of these schemes, even in their unlimited form, as we will see in the numerical applications presented below.

As far as we are proposing to use the unlimited version, it makes sense to find the choices of β that maximize the compression factor, going beyond the ansatz (19). Higher values of b_{max} can be actually obtained by a detailed case-by-case study of the original TVD conditions (16, 17). For instance, by reordering the terms in (17) we get

$$D_{j-1/2} \equiv 1 + \sum_{k=-m+1}^{m} (d_{k-1}^{m} - d_{k}^{m}) \, \frac{df_{j+k-1/2}^{+}}{df_{j-1/2}^{+}} \; \geq \; 0 \; , \tag{21}$$

where we assume $d_{k}^{m} = 0$ when $|k| \geq m$. A sufficient condition for (21) to hold is

$$1 + d_{-1}^{\;m} - d_{0}^{\;m} + b \sum_{k \neq 0} min(d_{k-1}^{m} - d_{k}^{m}, 0) \; \geq \; 0 \; , \tag{22}$$

6

which actually refines the former condition (20). The same reasoning shows that, allowing for (11), a sufficient condition for (18) to hold is:

$$\lambda_j \frac{\Delta t}{\Delta x} \left[d_{-1}^{\ m} - d_0^{\ m} + b \sum_{k \neq 0} max(d_{k-1}^{\ m} - d_k^{\ m}, 0) \right] \leq 1/2 . \tag{23}$$

For the simpler non-trivial cases we have (decreasing k order):

$$d_k^{\ 2} = \left(\beta - \frac{1}{12}, \ \frac{1}{2} - 2\beta, \ \beta + \frac{1}{12} \right) \tag{24}$$

$$d_k^{\ 3} = \left(\frac{1}{60} - \beta, \ 4\beta - \frac{7}{60}, \ \frac{1}{2} - 6\beta, \ 4\beta + \frac{7}{60}, \ -\frac{1}{60} - \beta \right) . \tag{25}$$

For $m = 2$, condition (22) leads then to:

$$b \leq 7/2 + 18\beta \qquad (\beta \leq \frac{1}{12}) \tag{26}$$

$$b \leq \frac{7 + 36\beta}{1 + 12\beta} \qquad (\frac{1}{12} \leq \beta \leq \frac{7}{36}) . \tag{27}$$

It follows that the optimal values for the third-order scheme are

$$\beta = \frac{1}{12} , \qquad b_{max} = 5 . \tag{28}$$

For the fifth-order scheme ($m = 3$), condition (22) leads instead to:

$$b \leq \frac{37 + 600\beta}{16} \qquad (\beta \leq \frac{1}{60}) \tag{29}$$

$$b \leq \frac{37 + 600\beta}{15 + 60\beta} \qquad (\frac{1}{60} \leq \beta \leq \frac{2}{75}) \tag{30}$$

$$b \leq \frac{37 + 600\beta}{7 + 360\beta} \qquad (\frac{2}{75} \leq \beta \leq \frac{37}{600}) . \tag{31}$$

It follows that the optimal values for the fifth-order scheme are

$$\beta = \frac{2}{75} , \qquad b_{max} = \frac{265}{83} . \tag{32}$$

Note that the ansatz (19) gives a smaller compression factor $b_{max} = 9/4$ and, more important, the optimal β value in this case is beyond the original bound $1/60$. Note also that the values of the compression parameter tend to diminish with the accuracy order of the algorithm. This suggests that higher-order cases $m > 3$ may not be so useful in the unlimited case.

4 Finite difference version

The linear flux-modification scheme described in the preceding section can be applied to any lower-order TVD flux. The case of the LLF flux (5) has actually been considered in [8]. Our objective here is to obtain a scheme which can be cast as a simple finite-difference algorithm, so that we will take advantage of the simplicity of the LLF flux (5), which can be written in flux-vector-splitting (FVS) form:

$$h_{j+1/2} = f_j^+ + f_{j+1}^- , \qquad f_j^{\pm} \equiv \frac{1}{2} \left[f_j \pm \lambda_{j\pm1/2} \, u_j \right] . \tag{33}$$

The FVS form (33), like the original one (5), is just first-order accurate. We will extend it to higher-order accuracy by means of the Osher-Chakrabarthy algorithm, as described in the previous sections. The flux differences (9) in this case get the simple form:

$$df_{j+1/2}^{\pm} = 1/2 \left[f_{j+1} - f_j \pm \lambda_{j+1/2} \left(u_{j+1} - u_j \right) \right] . \tag{34}$$

The linear character of this formula allows to get a compact finite-difference expression for the whole scheme. Allowing for (34), the semi-discrete algorithm (8) can be written as

$$\partial_t u_j = -C^{2m} f_j + (-1)^{m-1} \beta (\Delta x)^{2m-1} D_+^m D_-^{m-1} (\lambda_{j-1/2} \, D_- u_j) , \tag{35}$$

which amounts to assume a $2m$th-order-accurate central difference operator acting on the flux terms plus a dissipation operator of order $2m$ depending on the spectral radius λ. As we will see below, the resulting finite-difference scheme (35) provides a cost-effective alternative for CFD simulations.

Let us remark here that the choices (28, 32) derived in the previous section are optimal for a generic choice of the lowest-order TVD Flux. In the LLF case (5), however, it is clear that the spectral radius can be multiplied by a global magnifying factor $K > 1$, while keeping the TVD properties. Allowing for the finite-difference form (35) of the unlimited version, magnifying λ amounts to magnify β, that is:

$$(\beta, \; K\lambda) \qquad \Leftrightarrow \qquad (K\beta, \; \lambda) . \tag{36}$$

It follows that the values of the compression factor b_{max} obtained in the previous section must be interpreted just as lower-bound estimates. In particular, the equivalence (36) implies that any compression factor bound obtained for a particular value β_0 applies as well to all values $\beta > \beta_0$. This agrees with

8

the interpretation of the second term in (35) as modelling numerical dissipation. On the other side, this dissipation term is actually introducing the main truncation error. We will use then in what follows the β values in (28, 32), which are still optimal in the sense that they provide the lower numerical error compatible with the highest lower-bound for the compression parameter.

5 One-dimensional numerical tests

We will test now the behavior of the centered finite-difference scheme (35) by means of some standard numerical experiments in one space dimension. We will use here the well-known method-of-lines (MoL) [16] in order to deal separately with the space and the time discretization. In every case, the time discretization will be implemented by the following strong-stability-preserving (SSP), 3rd-order-accurate, Runge-Kutta algorithm [17]:

$$
\begin{aligned}
u^* &= E(u^n) \\
u^{**} &= \frac{3}{4}\, u^n + \frac{1}{4}\, E(u^*) \\
u^{n+1} &= \frac{1}{3}\, u^n + \frac{2}{3}\, E(u^{**}) \; ,
\end{aligned}
\tag{37}
$$

where $E(u)$ is the basic Euler step, that is

$$
E(u_j) = u_j + \Delta t \, (\partial_t\, u_j) \, ,
\tag{38}
$$

and $\partial_t\, u_j$ is computed by the finite difference formula (35).

5.1 Advection equation

Let us start by the scalar advection equation. This is the simplest linear case, but it allows to test the propagation of arbitrary initial profiles, containing jump discontinuities and corner points, departing from smoothness in many different ways. This is the case of the Balsara-Shu profile [11], which will be evolved with periodic boundary conditions.

We compare in Fig. 1 the numerical result with the exact solution after a single round trip, for two different resolutions. The third-order five-points formula from the proposed class (35) has been used with $\beta = 1/12$ in both cases. The propagation speed in the simulation agrees with the exact one, as expected for a third-order-accurate algorithm. The smooth regions are described correctly: even the height of the two regular maxima is not reduced too much
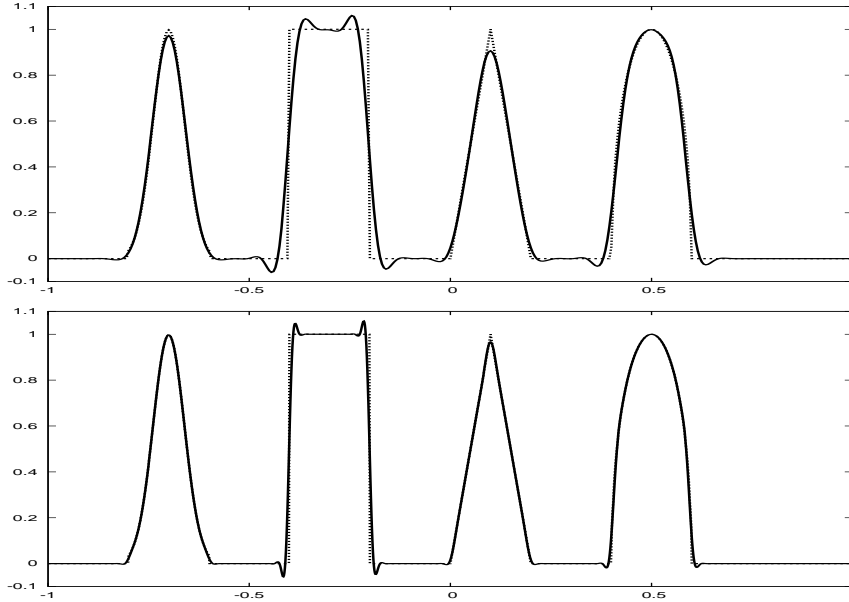
Fig. 1. Advection of the Balsara-Shu profile in a numerical mesh of either 400 points (upper panel) or 800 points (lower panel). A third-order scheme ($m = 2$, $\beta = 1/12$) is used in both cases. The results are compared with the initial profile (dotted line) after a single round-trip.

by dissipation, as expected for an unlimited algorithm with just fourth-order dissipation. There is a slight smearing of the jump slopes, as usual for contact discontinuities, which gets smaller with higher resolution.
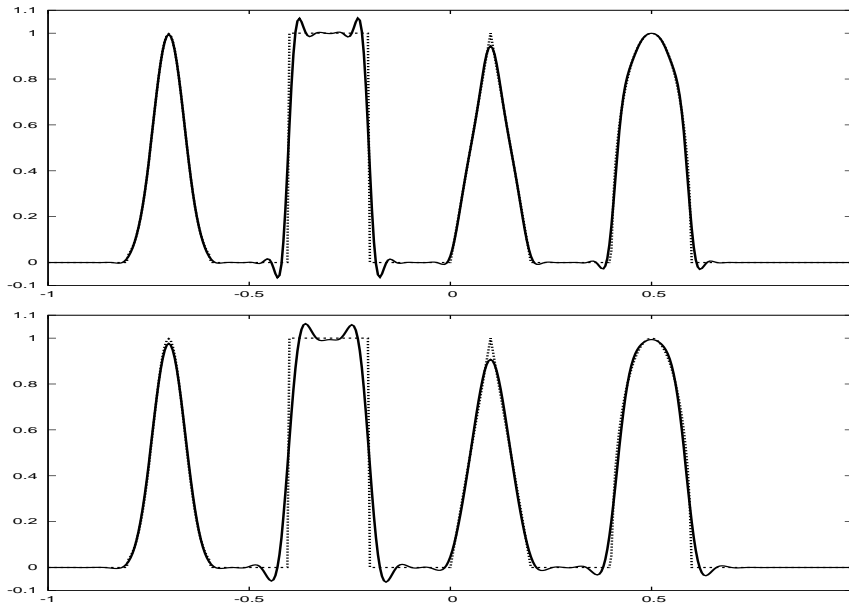

Fig. 2. Same as in Fig. 1, but using a fifth-order scheme ($m = 3$) with $\beta = 2/75$ (upper panel). In the lower panel we show the results after ten round-trips. The same settings are used in both cases.
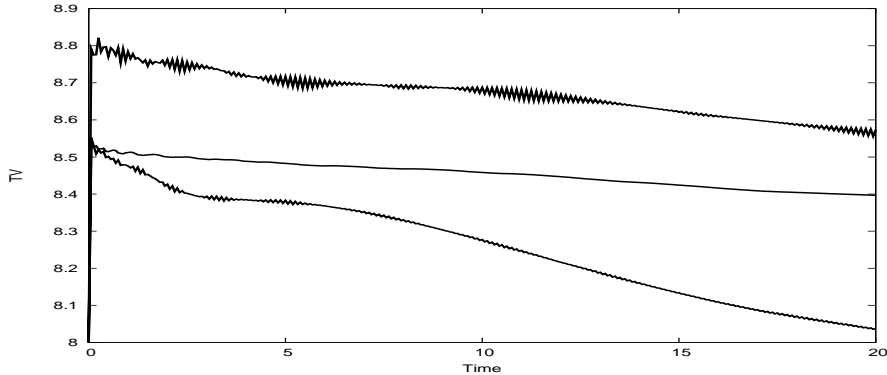
Fig. 3. Advection equation. Time evolution of the total variation. The horizontal axis corresponds to the exact solution: $TV(u) = 8$. From top to bottom: $m = 3$ scheme with 400 points, $m = 2$ scheme with 800 points, and $m = 2$ scheme with 400 points. After the initial increase, which depends on the selected method, the TV tends to diminish. Increasing resolution just reduces the TV diminishing rate.

Concerning monotonicity, it is clear that the total variation of the initial profile has increased by the riddles besides the corner points and, more visibly, near the jump discontinuities. By comparing the two resolutions, we see that the height of the overshots does not change. This means that, as in the case of the Gibbs phenomenon, there is no convergence by the maximum norm, although convergence by the L_2 or similar norms is apparent from the results. On the other hand, it is clear that the total variation is bounded for this fixed time, independently of the space resolution or, equivalently, the time step size. This is precisely the requirement for TVB.

We show in Fig. 2 the same simulation, in a 400 points mesh, for the fifth-order method ($m = 3$, $\beta = 2/75$). In the upper panel, corresponding to a single round-trip, we can see that one additional riddle appears at every side of the critical points, due to the larger (seven point) stencil. We show also in the lower panel the results of the same simulation after ten round-trips. The cumulative effect of numerical dissipation is clearly visible: the extra riddles tend to diminish. The total variation is not higher than the one after a single round trip. This statement can be verified by plotting, as we do in Fig. 3, the time evolution of $TV(u)$ for the different cases considered here. In all cases, a sudden initial increase is followed by a clear diminishing pattern. These numerical results indicate that the bound on the total variation is actually time-independent, beyond the weaker TVB requirement.

5.2 Burgers equation

Burgers equation provides a simple example of a genuinely non-linear scalar equation. A true shock develops from smooth initial data. We will compute
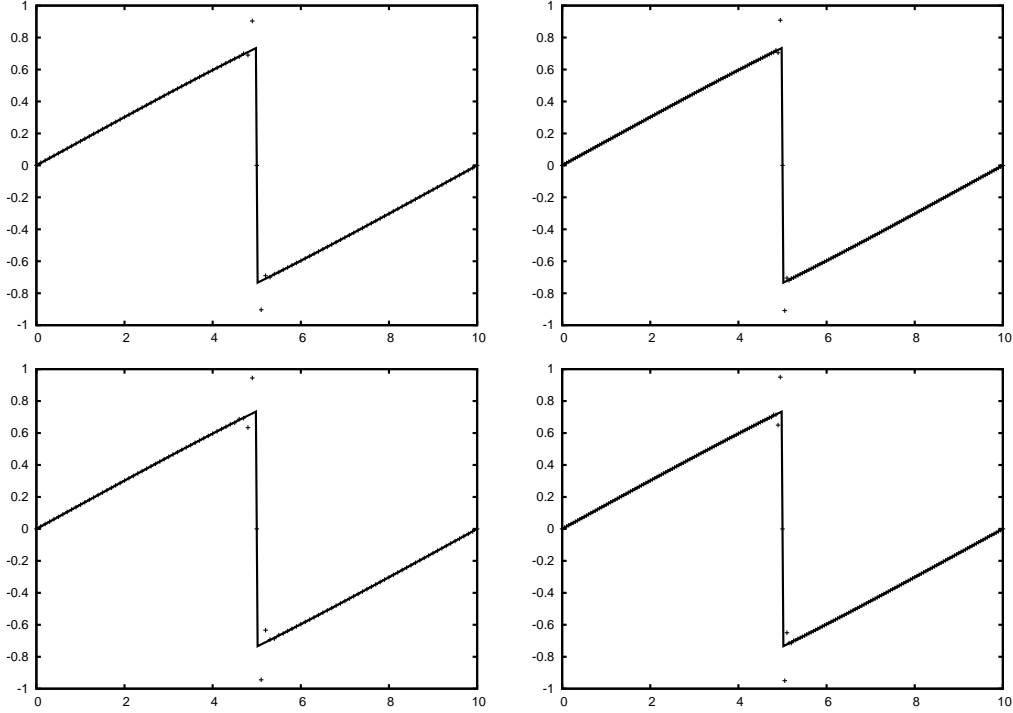
11

Fig. 4. Burgers equation: evolution of an initial sinus profile. The numerical solution (point values) is plotted versus the exact solution (continuous line), for 100 points and 200 points resolution (left and right panels, respectively) and for the $(m = 2, \beta = 1/12)$ and the $(m = 3, \beta = 2/75)$ schemes (upper and lower panels, respectively).

here the evolution of an initial sinus profile, with fixed boundary conditions. We plot in Fig. 4 the numerical solution values versus (the principal branch of) the exact solution, at the time where the shock has fully developed. We compare 100 points with 200 points resolution (left and right panels, respectively), and also the 3rd-order and 5th-order schemes described previously (upper and lower panels, respectively). Concerning the resolution effect, we can see here again that the spurious oscillations affect mainly the points directly connected with the shock, in a number depending on the stencil size but independent of the resolution.

These conclusions are fully confirmed by a second simulation, obtained by adding a constant term to the previous initial profile, that is

$$u(x) = \frac{1}{2} + sin(\frac{x\,\pi}{5})\,, \tag{39}$$

with periodic boundary conditions. We can see in Fig. 5 that a shock again develops, but it does no longer stand fixed: it propagates to the right. Note that the plot shown corresponds to $t = 7$. We can confirm in this case that both the number of spurious riddles and the magnitude of the overshots do
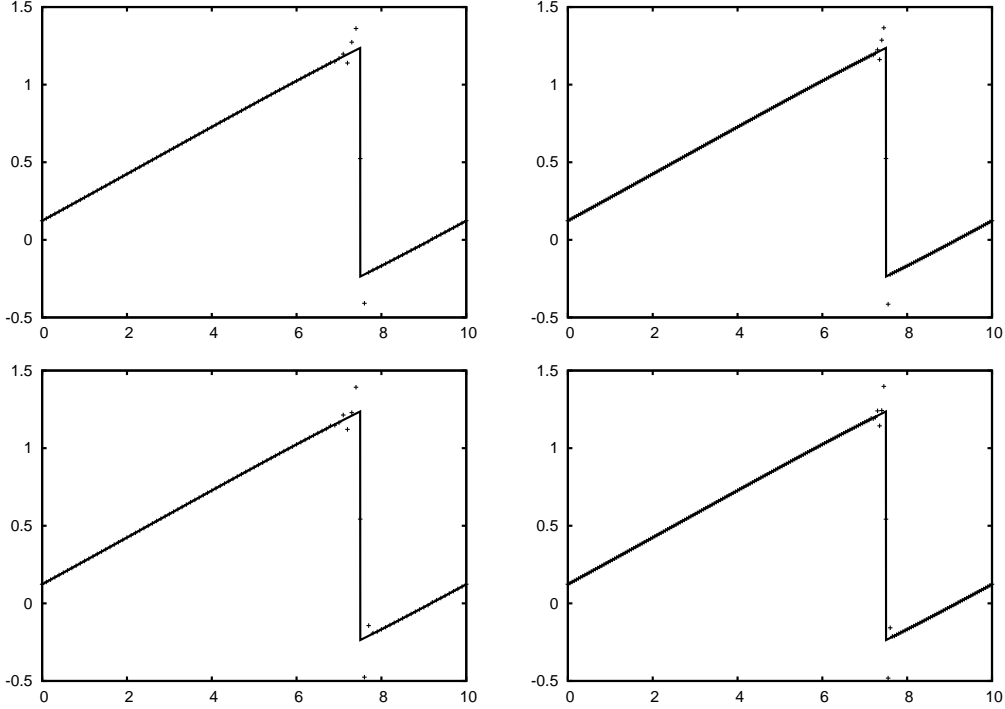
12

Fig. 5. Same as in the previous figure, but now for a moving sinus profile. The numerical solution (point values) is plotted versus the exact solution (continuous line), for 100 points and 200 points resolution (left and right panels, respectively) and for the ($m = 2$, $\beta = 1/12$) and the ($m = 3$, $\beta = 2/75$) schemes (upper and lower panels, respectively).

not increase with resolution, although it is larger in this case than in the static shock one. We can confirm also that these effects increase with the order-of-accuracy of the scheme: the larger stencil adds one more riddle at every side and slightly larger overshots.

These results clearly indicate convergence in the L_1 or similar norms (but of course not in the maximum norm). Let us actually perform a convergence test by considering the initial profile [18]

$$u(x, 0) = 1 + \frac{1}{2} \, sin(\pi \, x) \,, \tag{40}$$

which is smooth up to $t = 2/\pi$. We show in Table 1 the errors at time $t = 0.3$, where the shock has not yet appeared. The first group of values corresponds to the third-order method, and this is confirmed by the data both in the L_1 and the L_∞ norms. The second group of values corresponds to the fifth-order method, but only third-order accuracy is obtained from the numerical values. This is because we keep using the third-order Runge-Kutta algorithm (37) for the time evolution. In order to properly check the space discretization accuracy, we include a third group of values, obtained with the same algorithm, but

13

with a much smaller time step in order to lower the time discretization error: the leading error term is then due to the space discretization and the expected fifth order accuracy is confirmed by the numerical results, although the L_∞ norm shows a slightly decreasing convergence rate for the higher resolution results.

Nx	L_1 error	L_1 order	L_∞ error	L_∞ order
160	7.22579 E-6	2.998	5.17334 E-5	2.981
320	9.04719 E-7	2.999	6.55306 E-6	2.994
640	1.13182 E-7	3.000	8.22735 E-7	2.998
1280	1.41486 E-8		1.03006 E-7	
160	1.44981 E-6	3.017	9.57814 E-6	2.981
320	1.79043 E-7	3.005	1.21318 E-6	2.997
640	2.23035 E-8	3.003	1.51957 E-7	2.999
1280	2.78216 E-9		1.90041 E-8	
160	7.09726 E-8	4.88	8.6567 E-7	4.97
320	2.41410 E-9	4.76	2.76804 E-8	3.98
640	8.92936 E-11	4.91	1.75192 E-9	3.48
1280	2.95859 E-12		1.36890 E-11	

Table 1

Burgers problem. Norm of the errors and convergence rate at $t = 0.3$ for the initial profile (40). The first group of values corresponds to the $m = 2$ method with $\Delta t = 0.6\Delta x$. The second group corresponds to the $m = 3$ method with the same time step. The third group corresponds again to the $m = 3$ method, but with $\Delta t = 0.06\Delta x$.

5.3 Buckley-Leverett problem

A more demanding test, still for the scalar case, is provided by the Buckley-Leverett equation which models two-phase flows that arise in oil-recovery problems [7]. This equation contains a non-convex (s-shaped) flux of the form

$$f(u) = \frac{4u^2}{4u^2 + (1 - u)^2} \, . \tag{41}$$

Non-convex fluxes can lead to compound shock waves which are shocks adjacent to a rarefaction wave with wave speed equal to the shock speed at the point of attachment.
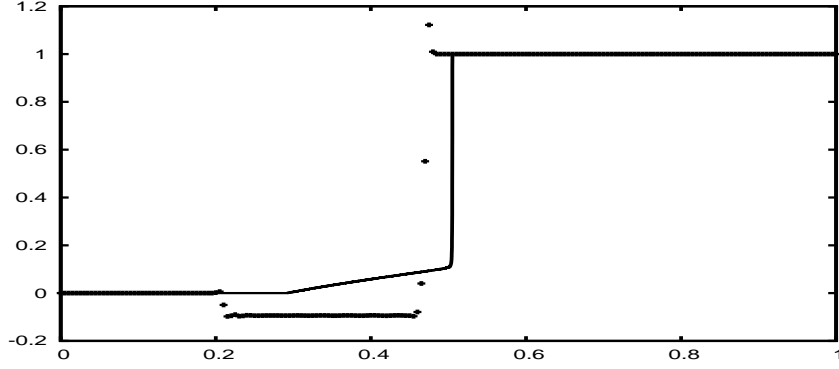
Fig. 6. Buckley-Leverett's problem. The continuous line corresponds to the LLF first-order algorithm, with 10.000 points, as a replacement for the exact solution. The crosses line corresponds to the third-order algorithm ($m = 2$, $\beta = 1/12$) with 200 points, converging towards a different solution.

We will perform first a simulation with the initial data

$$u(x) = \begin{cases} 0 & 0 \leq x < 1 - 1/\sqrt{2} \\ 1 & 1 - 1/\sqrt{2} \leq x < 1 \end{cases} \tag{42}$$

so that the inflexion point in the flux (41) lies inside the interval spanned by the data.

The exact solution in this case is well approximated by a very-high-resolution (10.000 points) simulation using the first-order LLF algorithm, as displayed in Fig. 6 (continuous line). We see a right-propagating compound shock wave, consisting of a shock followed by a rarefaction wave, which propagates in the same direction. The results for our third-order algorithm, represented by the crosses line in Fig. 6, fail to reproduce correctly the rarefaction wave, which
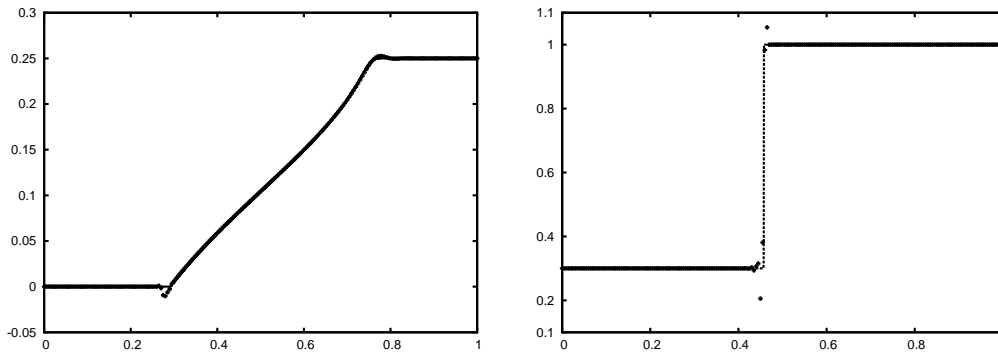

Fig. 7. Same as in the previous figure, but now for two different dynamical ranges, which avoid the flux inflexion point. In the left panel, an ordinary rarefaction wave appears, which is correctly modelled by the third-order algorithm. In the right panel, a simple shock appears, well captured by the third-order algorithm.

15

is replaced by an spurious intermediate state, resulting into a slower shock propagation speed.

In order to single out the problem, we have performed simulations for the same flux (41) but with a dynamical range that avoids the inflexion point either from below or from above. The results are plotted in Fig. 7, where we see either an ordinary rarefaction wave (left panel) or a simple shock (right panel), but no compound shock. In both cases, the third-order algorithm ($m = 2$, $\beta = 12$) is able to model correctly the dynamics. This results indicate that the problem with compound shocks can be triggered by the presence of overshots at the connection point between the shock and the associated rarefaction wave, which can break the compound structure. The TVD character of the LLF flux prevents this problem to arise, as it is clearly shown in Fig. 6 (continuous line).

5.4 Euler equations

Euler equations for fluid dynamics are a convenient arena for testing the proposed schemes beyond the scalar case. In the ideal gas case, we can check the numerical results against well-known exact solutions containing shocks, contact discontinuities and rarefaction waves. We will deal first with the classical
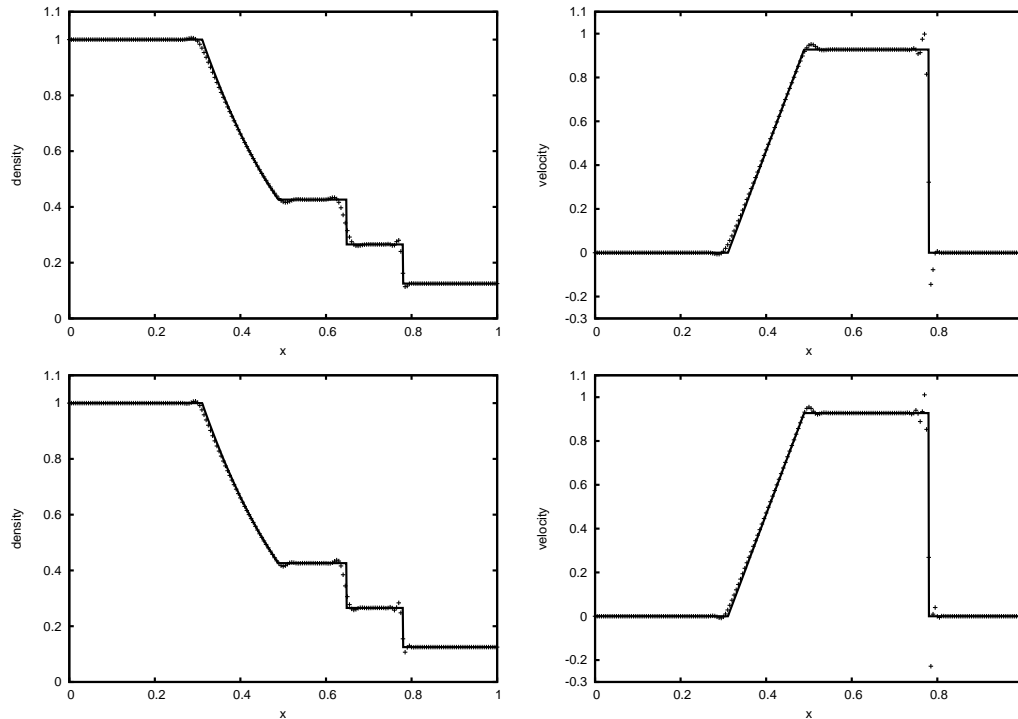

Fig. 8. Sod shock tube problem. Density and speed profiles (left and right panels, respectively), for the ($m = 2$, $\beta = 1/12$) and the ($m = 3$, $\beta = 2/75$) schemes (upper and lower panels, respectively).

16

Sod shock-tube test [19] with a standard 200 points resolution.

We plot in Fig. 8 the gas density and speed profiles (left and right panels, respectively). Looking at the 3rd-order scheme results (upper panels), we see that both the rarefaction wave and the shock are perfectly resolved, whereas the contact discontinuity is smeared out. As a consequence, the main overshots are just besides the shock, specially visible in the speed profile, where the jump is much higher. Concerning the 5th-order scheme (lower panels), the contact discontinuity is slightly better resolved. This is however at the price of extra riddles and more visible overshots, so that the 3rd-order scheme seems to be more convenient.

A more demanding test is obtained when assuming a discontinuity in the initial speed, as in the Lax test [20]. As we see in Fig. 9, we get the same behavior than for the Sod test case. The main difference is that the density jump at the contact discontinuity is much higher: the smearing of the density profile there is more visible, in contrast with the sharp shock profile nearby. Note also that some speed overshots are greater than the ones arising in the Sod test case (we have kept here the same 200 points resolution for comparison). The third-order algorithm seems to be more convenient again in this case.
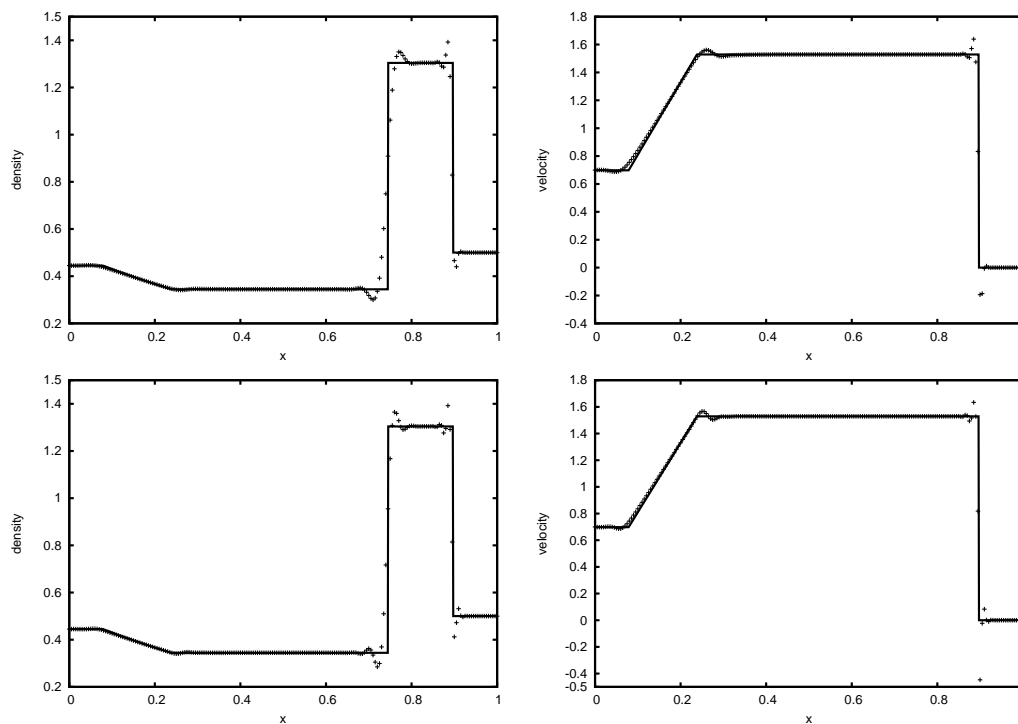

Fig. 9. Lax shock tube problem. Density and speed profiles (left and right panels, respectively), for the ($m = 2$, $\beta = 1/12$) and the ($m = 3$, $\beta = 2/75$) schemes (upper and lower panels, respectively).

6 Multidimensional tests

The results of this paper can be extended to a multidimensional case in a simple way. The semi-discrete equation (3) can be written in a rectangular grid as follows:

$$\partial_t u_{i,j} = -\frac{1}{\Delta x}\left(f_{i+1/2,j} - f_{i-1/2,j}\right) - \frac{1}{\Delta y}\left(f_{i,j+1/2} - f_{i,j-1/2}\right), \qquad (43)$$

and the numerical flux can be computed by applying (10) to every single direction. Note however that the restriction (23) on the time step must be extended in this case to

$$\lambda_j \, \Delta t \, \left(\frac{1}{\Delta x} + \frac{1}{\Delta y}\right)\left[\, d_{-1}^{\,m} - d_0^{\,m} + b \sum_{k\neq 0} max(d_{k-1}^{\,m} - d_k^{\,m}, 0)\,\right] \ \le \ 1/2\,. \quad (44)$$

In the finite-difference version (35), the extension to the multidimensional case amounts to replicate the right-hand-side difference operators for every single direction: no cross-derivative terms are required. This multidimensional extension allows to deal with some MHD tests, which add more complexity to the dynamics, clearly beyond the simple tests considered in the previous section.

6.1 The Orszag-Tang 2D vortex problem

As a first multi-dimensional example, let us consider here the Orszag-Tang vortex problem [21]. This is a well-known model problem for testing the transition to supersonic magnetohydrodynamical (MHD) turbulence and has become a common test of numerical MHD codes in two dimensions.

A barotropic fluid ($\gamma = 5/3$) is considered in a doubly periodic domain $[0, 2\pi]^2$, with uniform density ρ and pressure p. A velocity vortex given by $\mathbf{v} = (-\sin y, \sin x)$, corresponding to a Mach 1 rotation cell, is superimposed with a magnetic field $\mathbf{B} = (-\sin y, \sin 2x)$, describing magnetic islands with half the horizontal wavelength of the velocity roll. As a result, the magnetic field and the flow velocity differ in their modal structures along one spatial direction.

In Fig. 10 (left panel) the temperature, $T = p/\rho$, is represented at a given time instant ($t = 3.14$). The figure clearly shows how the dynamics is an intricate interplay of shock formation and collision. The numerical scheme, with $m = 2$ and $\beta = 1/12$ seems to handle the Orszag-Tang problem quite well. In Fig. 10
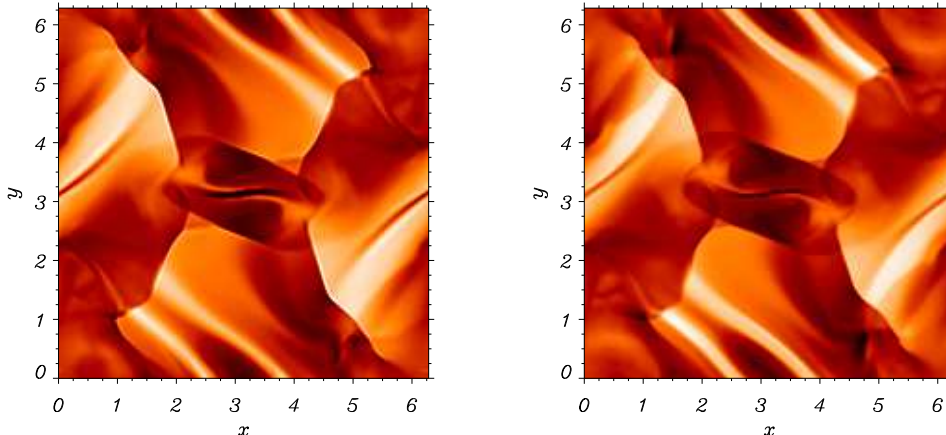
Fig. 10. Temperature at $t = 3.14$ in the Orszag-Tang vortex test problem. In this simulation the grid has 200×200 mesh points. In the left panel the third-order scheme ($m = 2$, $\beta = 1/12$) has been used while in the right panel the result is for a a second order scheme built from the Roe-type solver and the MC limiter.

(right panel) we plot the results for the same problem using a second order scheme built from the Roe-type solver and the monotonized-central (MC) symmetric limiter [22]. The results with both methods are qualitatively very similar.

6.2 Torrilhon MHD shock tube problem

We now consider the MHD shock tube problem described by Torrilhon [23] to investigate dynamical situations close to critical solutions. We will assume again a barotropic fluid with $\gamma = 5/3$. The initial conditions for the components of the magnetic field (B_2, B_3) are $(\cos\theta, \sin\theta)$, with $\theta = 0$ for $x \leq 0$. Depending on the angle θ between the left and right transverse components of the magnetic field, different types of solutions are found. Regular r-solutions consist only of shocks or contact discontinuities. Critical c-solutions appear in the coplanar case, where the angle θ is an integer multiple of π. These solutions can contain also non-regular waves, such as compound waves.

We consider the situation for an *almost* co-planar case, $\theta = 3$. Analytically, this has a regular r-solution, but the numerical solution is attracted towards the nearby critical solution for $\theta = \pi$. Fig. 11 shows the density profile plotted together with the correct r-solution (solid black line) and the co-planar c-solution (dashed line). The r-solution has, from left to right, a rarefaction, a rotation, a shock, a contact discontinuity, a shock, a rotation and a rarefaction. The discrepancies among the different solutions are mainly in the interval $[-0.35, -0.1]$.
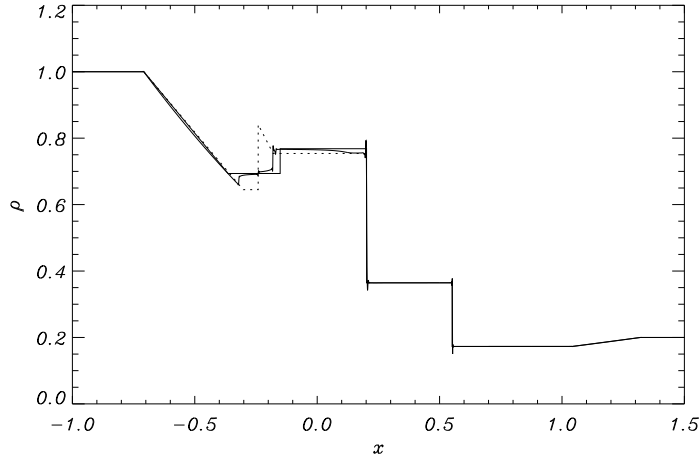
Fig. 11. Plot of the density ρ at $t = 0.4$ for the almost co-planar problem with $\theta = 3$. In this simulation 5000 mesh points have been used. The dashed line represents the critical c-solution while the solid black line is the correct r-solution. Both solutions differ clearly in the interval $[-0.35, -0.1]$. The numerical simulation lies between the two.
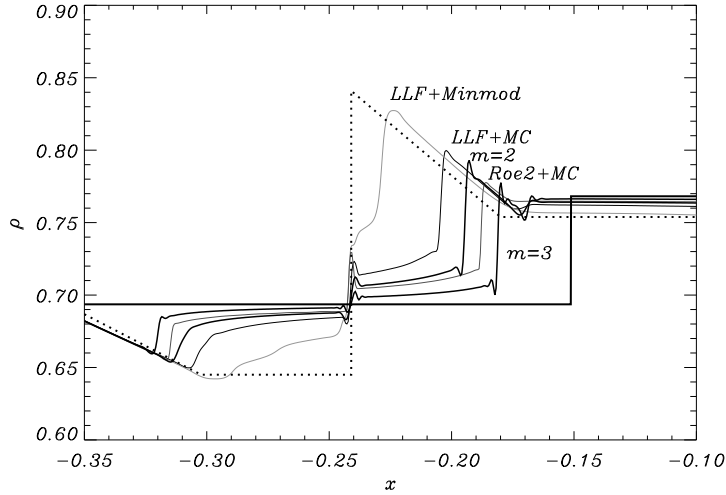

Fig. 12. Same as Fig. 11, but enlarging the interval where the discrepancies show up. In addition to the exact regular and critical solutions, we plot, from top to bottom, the simulations for schemes using LLF with minmod limiter, LLF with MC limiter, the unlimited $m = 2$ algorithm, a Roe solver with MC limiter and the unlimited $m = 3$ algorithm.

This interval is magnified in Fig. 12. The solid black line is the correct r-solution while the dashed line represents the critical c-solution. We see that the solutions with $m = 2$ and $m = 3$ tend to the correct solution although they keep some remnant from the c-solution. For comparison purposes we have also represented the numerical solution obtained with other schemes. We have used a second order LLF scheme and a second order Roe solver with either

20

the minmod or the MC slope limiters.

The LLF scheme with the minmod limiter gets too close to the c-solution, even for this high-resolution simulation. The situation improves by replacing the minmod limiter by the MC one, but still gets farther from the right solution than the schemes proposed in this paper. Only the combination of a Roe-type solver with the MC limiter improves the results of the third-order scheme ($m = 2$), but not those of the fifth-order scheme ($m = 3$). This problem provides one specific example in which the fifth-order scheme seems to be more convenient than the third order one: the extra riddles are actually compensated by a clear improvement in the solution accuracy.

6.3 Double Mach reflection problem

This problem is a standard test case for high-resolution schemes. It corresponds to an experimental setting in which a shock is driven down a tube which contains a wedge. We will adopt here the standard configuration proposed by Woodward and Colella [24], involving a Mach 10 shock in air ($\gamma = 1.4$) at a 60° angle with a reflecting wall. The air ahead of the shock is stationary with a density of 1.4 and a pressure of 1. The reflecting wall lies at the bottom of the computational domain, starting at $x = 1/6$. Allowing for this, the exact post-shock condition is imposed at the bottom boundary in the region $0 \le x \le 1/6$ and a reflecting wall condition is imposed for the rest. Inflow (post-shock) conditions are used at the left and top boundaries, whereas an outflow (no gradient) condition is used for the right boundary.
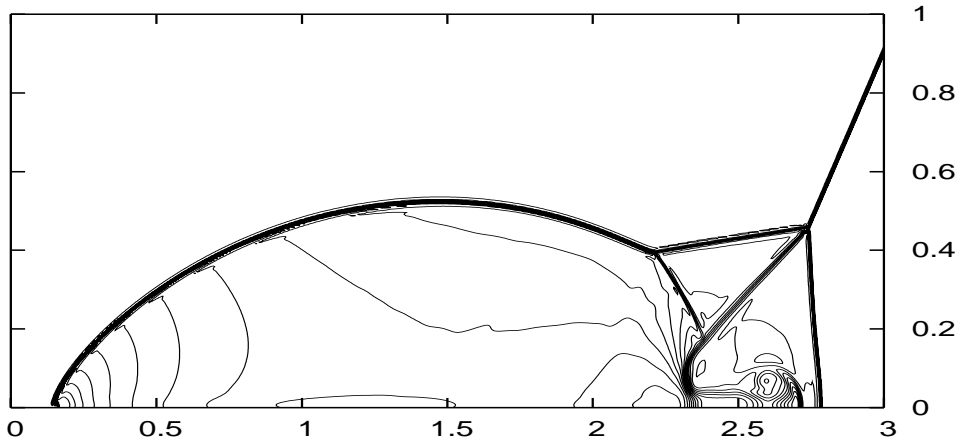

Fig. 13. Double Mach reflection. Density plot at $t = 0.2$. The simulation is made with the 3rd-order method ($m = 2$, $\beta = 1/12$) with $\Delta x = \Delta y = 1/240$. 30 evenly spaced density contours are shown.
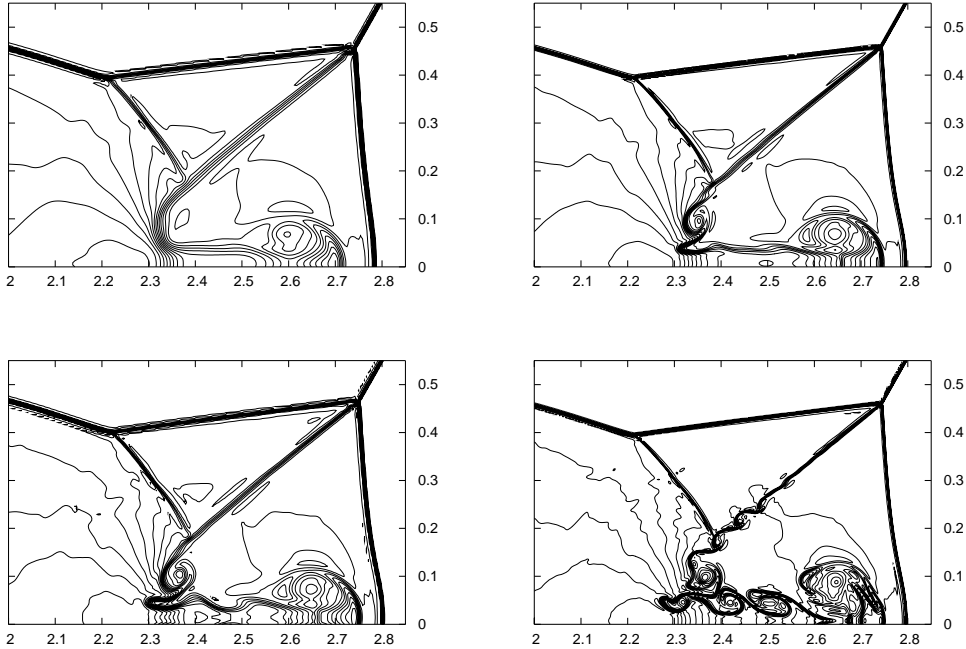
Fig. 14. Same as Fig. 13, but enlarging the lower right corner. The top panels correspond to the third-order method ($m = 2$, $\beta = 1/12$), with resolution of either 1/240 (left) or 1/480 (right). The bottom panels show the same for the 5th-order method ($m = 3$, $\beta = 2/75$). Both the jet near the bottom wall and the weak shock, generated at the kink in the main reflected shock, are well resolved. A vortex structure at the bottom of the diagonal contact discontinuity shows up, with more details appearing when increasing accuracy.

This configuration leads to a complex flow structure, produced by a double Mach reflection of the shock at the wall. A self-similar flow develops as the fluid meets the reflecting wall. Two Mach stems develop, with two contact discontinuities. We have plotted in Fig. 13 the density contours at $t = 0.2$, when the main features have fully developed. The more challenging ones are the jet propagating to the right near the reflecting wall and the weak shock generated at the second Mach reflection, as seen in the enlarged area in Fig. 14.

Our third-order results agree with the original ones [24] for the corresponding resolution: both the jet and the weak shock are clearly captured. Increasing both the resolution and the order-of-accuracy of the numerical algorithm, as shown in the subsequent panels in Fig. 14, we see more details of the jet rolling-up. Also, a vortex structure appears near the bottom wall, which starts affecting the diagonal contact discontinuity arising from the triple point. These high-resolution features, appearing in the last panel in Fig. 14, agree with the ones obtained with a WENO method of the same order (but double resolution, 1/960) in Ref. [25]. This also agrees with the results of recent spectral (finite) volume simulations [26], in which those structures show up gradually, as one is

getting more accurate simulations. This is another example in which a higher-order algorithm can be preferred, as it captures more detailed features of complex structures for a given resolution.

7 Conclusions and outlook

The numerical experiments presented in this paper provide clear evidence for a TVB behavior of the proposed schemes. This means that the total variation growth is uniformly bounded, independently of the resolution, for a fixed evolution time. Moreover, the experimental pattern is a sudden growth of the total variation, which provides a time-independent bound for the rest of the evolution. This growth is confined to the mesh points directly connected with non-sonic critical points, especially near discontinuities. But the resulting riddles do not spread over smooth regions and the overall features of the solution are preserved as a result. In the case of compound shocks, however, the numerical simulations actually mystify the physical solution: the spurious riddles affect the contact point between the shock and the adjacent rarefaction wave, breaking the compound structure, even if the TVB behavior is still preserved.

The proposed schemes are obtained from the unlimited version of the Osher-Chakrabarthy [6] linear flux-modification algorithms. The robustness of the unlimited version is related with the high compression factor of this algorithms family. We have actually improved the available estimates up to a remarkable value of $b = 5$, for the third-order case. This suggests that these estimates could be even improved by using alternative bound-setting procedures. Unfortunately, even in the scalar case, we are not able to prove rigorously the TVB properties of these methods, although we are currently working in this direction.

We have combined the unlimited Osher-Chakrabarthy algorithm with the simple LLF flux formula. As a result, we have been able to derive the compact finite-difference scheme (35), which is equivalent to the corresponding finite-volume implementation in the unlimited case. This provides an extremely cost-efficient algorithm for dealing with the most common problems, even in presence of interacting dynamical shocks, as we have done in the Orszag-Tang 2D vortex and the double Mach reflection cases. Of course, its use should be limited to convex-flux problems, where compound shocks do not arise.

The resulting finite-difference formula (35) is similar to the ones obtained by the 'artificial viscosity' approach (see for instance ref. [27]). The main difference is that the spectral radius plays a key role here in the dissipation term, providing some sort of 'adaptive viscosity'. Even in the most simple constant-speed case we can still see that the order of accuracy in our case

is dictated by the dissipation term, in contrast with the extra freedom one gets in the standard artificial viscosity approach. Moreover, our compression factor estimates provide specific prescriptions for the value of the dissipation coefficient.

References

[1] P. D. Lax, B. Wendroff (1960), "Systems of conservation laws". Commun. Pure Appl Math. 13: 217-237.

[2] R. W. MacCormack (1969), "The Effect of viscosity in hypervelocity impact cratering". AIAA Paper 69-354.

[3] S. K. Godunov (1959), "A Difference Scheme for Numerical Solution of Discontinuos Solution of Hydrodynamic Equations". Math. Sbornik 47: 271-306, translated US Joint Publ. Res. Service, JPRS 7226, (1969).

[4] V. V. Rusanov (1961), "Calculation of Intersection of Non-Steady Shock Waves with Obstacles". J. Comput. Math. Phys. USSR 1: 267-279.

[5] A. Harten (1983), "High Resolution Schemes for Hyperbolic Conservation Laws". J. Comput. Phys. 49: 357-393.

[6] S. Osher and S. Chakravarthy (1984), "Very High Order Accurate TVD schemes", ICASE Report 84-44, IMA Volumes in Mathematics and its Applications vol 2: 229-274. Springer-Verlag, 1986.

[7] R. J. LeVeque (1992), "Numerical Methods for Conservation Laws", Lectures in Mathematics, Birkhäuser.

[8] Chi-Wang Shu (1987), "TVB Uniformly High-Order Schemes for Conservation Laws", Mathematics of Computation 49:105-121.

[9] A. Harten and S. Osher (1987), "Uniformly high-order accurate nonoscillatory schemes, I", SIAM J. Num. Anal. 24:279-309

[10] A. Harten, B. Engquist, S. Osher and S. Charavarty (1987), Uniformly high-order accurate essentially non-oscillatory schemes", J. Comp. Phys. 71:231-303.

[11] D. S. Balsara and Chi-Wang Shu (2000), "Monotonicity preserving weighted essentially non-oscillatory schemes with increasingly high order of accuracy", J. Comp. Phys. 160:405-452.

[12] Doron Levy, Gabriella Puppo and Giovanni Russo (2000), "A third order central WENO scheme for 2D conservation laws", Applied Numerical Mathematics 33:415.

[13] Steve Bryson and Doron Levy (2006), "On the total variation of High-Order Semi-Discrete Central schemes for Conservation Laws", Journal of Scientific Computation 27:163.

[14] A. Kurganov and E. Tadmor (2000), "New High-Resolution Central Schemes for Nonlinear Conservation Laws and Convection-Diffusion Equations", J. Comp. Phys. 160:214-282.

[15] A. Kurganov and Doron Levy (2000), "A Third-Order Semidiscrete Central Scheme for Conservation Laws and Convection-Diffusion Equations", SIAM J. Sci. Comput. 22:1461-1488.

[16] O. A. Liskovets (1965), Differential equations I 1308-1323.

[17] C.-W. Shu and S. Osher (1988), "Efficient implementation of essentially non-oscillatory shock-capturing schemes", J. Comp. Phys. v77:439-471.

[18] Xu-dong Liu and S. Osher (1996), "Nonoscillatory High Order Accurate Self-Similar Maximum Principle Satisfying Shock Capturing Schemes I", SIAM J. Numer. Anal. 33:439-471.

[19] G. A. Sod (1978), "A Survey of Several Finite Difference Methods for Systems of Nonlinear Hyperbolic Conservation Laws". J. Comput. Phys. 27:1-31.

[20] P. D. Lax (1954), "Weak solutions of nonlinear hyperbolic equations and their numerical computation", Comm. Pure Appl. Math. 7:159193.

[21] S. A. Orszag and C. M. Tang (1979), "Small-scale structure of two-dimensional magnetohydrodynamic turbulence". J. Fluid Mech. 90, 1:129-143.

[22] B. Van Leer (1977), "Towards the ultimate conservative difference scheme III. Upstream-centered finite-difference schemes for ideal compressible flow". J. Comp. Phys. 23: 263-75.

[23] M. Torrilhon (2003), "Non-uniform convergence of finite volume schemes for Riemann problems of ideal magnetohydrodynamics". J. Comput. Phys. 192: 73-74.

[24] P. Woodward and P. Colella (1984), "The numerical simulation of two-dimensional fluid flow with strong shock". J. Comput. Phys. 54: 115173.

[25] J. Shi, Y-T. Zhan, and C-W. Shu (2003), "Resolution of high-order WENO schemes for complicated flow structures", J. Comput. Phys. 186: 690696.

[26] Z. J. Wang, L. Zhang and Y. Liu (2004), "Spectral finite volume method for conservation laws on unstructured grids IV: extension to two-dimensional systems", J. Comput. Phys. 194: 716741.

[27] B. Gustafsson, H. O. Kreiss and J. Oliger (1995), "Time Dependent Problems and Difference Methods". Wiley-Interscience (New York).